The 9th European Congress on Computational Methods in Applied Sciences and Engineering
ECCOMAS Congress 2024
3–7 June 2024, Lisboa, Portugal

DATA-DRIVEN CALIBRATION OF RANS TRANSITION MODELS WITH DEEP LEARNING ECCOMAS CONGRESS 2024

J. CAPEL-JORQUERA[1,3], M. CHÁVEZ-MÓDENA[2,3], E. VALERO[2,3], AND L. M. GONZÁLEZ[1,3]

[1] CEHINAV, ETSIN
Universidad Politécnica de Madrid (UPM)
Av. de la Memoria, 4, 28040 Madrid, Spain
e-mail: j.capel@upm.es

[2] ETSIAE
Universidad Politécnica de Madrid (UPM)
Plaza Cardenal Cisneros 3, 28040 Madrid, Spain

[3] Center for Computational Simulation
Universidad Politécnica de Madrid (UPM)
Campus de Montegancedo, Madrid 28660, Spain

Key words: Computational Fluid Dynamics, CFD, Laminar to Turbulent Transition, Turbulence Modeling, Calibration, Deep Learning

Summary. This study presents a novel framework that leverages deep neural networks to optimize the parameters of Reynolds-Averaged Navier-Stokes (RANS) transition models, achieving precise alignment with experimental data. Our approach, validated using the 1-Equation γ transition model and the comprehensive ERCOFTAC T3 flat plate experiment series, systematically identifies the optimal set of parameters to minimize errors in predicting the skin friction coefficient evolution and the transition location along the flat plate for the T3A experiment. An extensive database is created through systematic parameter variation, which is then used to train a fully connected neural network to accurately predict skin friction distributions. The trained network then addresses the inverse problem, pinpointing the parameter set that best matches experimental measurements. This framework enhances the predictive accuracy of state-of-the-art RANS transition models and lays the foundation for an automated tool that streamlines parameter calibration, reducing manual effort and enabling more accurate simulations of complex transitional phenomena. The proposed approach offers significant potential for improving the reliability of simulations in aerospace and other engineering applications where transition prediction is crucial.

1 INTRODUCTION

The transition from laminar to turbulent flow has a significant impact on the aerospace industry, affecting various aspects of aircraft and spacecraft performance. Advances in natural laminar flow (NLF) wing technology have demonstrated that maintaining a laminar boundary layer can be highly beneficial, as laminar skin friction can be up to 90% lower than turbulent

skin friction at the same Reynolds number [13]. Various studies suggest that applying laminar flow control to large commercial aircraft can reduce aerodynamic drag by approximately 10% [6].

NLF wings are crucial not only for fixed-wing aircraft but also for rotorcraft and hypersonic systems. In rotorcraft, boundary layer transition influences hover capabilities and the overall performance envelope of new designs [12]. Small-scale Unmanned Aerial Systems (UASs) are expected to operate primarily in transitional flow regimes, where accurate prediction and control of transition can improve their efficiency and noise characteristics [1]. Additionally, the state of the boundary layer directly affects trailing-edge noise, a critical concern for both fixed-wing and rotary-wing aircraft.

In hypersonic systems, the transition from laminar to turbulent flow significantly affects surface heating, a critical factor in vehicle design due to its impact on thermal protection systems [24]. Furthermore, transitional shock-boundary layer interactions (SBLI) can introduce large unsteady loads, impacting vehicle stability and control effectiveness.

In the field of computational fluid dynamics (CFD), accurately capturing transition phenomena often requires scale-resolving simulations such as Large Eddy Simulations (LES) or Direct Numerical Simulations (DNS). However, these methods are computationally prohibitive, particularly at high Reynolds numbers. As a more practical alternative, Reynolds-Averaged Navier-Stokes (RANS) transition models have been developed. These models do not aim to replicate the detailed physics of transition but rather to provide adequate and accurate predictions at a significantly reduced computational cost. RANS models achieve this by incorporating empirical correlations as additional equations in the turbulence closure problem. These correlations involve numerous adjustable parameters or constants, which are typically calibrated based on a limited set of simple test cases. Consequently, the accuracy of these models often degrades when applied to more complex flow scenarios. The most widely used RANS transition models include:

- The $\gamma - Re_\theta$ transition model developed by Langtry [16]. This model is coupled with the widely extended $k - \omega\, SST$ turbulence model [15], and uses two additional transport equations for intermittency (γ) and the transition onset Reynolds number (Re_{θ_t}).

- The intermittency-based transition models developed by Menter [18][19]. These models are coupled with the $k-\omega\, SST$ turbulence model [15] and focus on modeling the intermittency of the transition process using a single extra transport equation for intermittency. They are simplified versions of the $\gamma - Re_\theta$ transition model by Langtry [16], maintaining Galilean invariance. The simplifications are achieved by omitting the Re_θ equation, reducing the complexity of the transition onset correlation, and even modeling the intermittency with an algebraic form, avoiding extra transport equations [19].

Several efforts have been made to enhance RANS transition models. Barrouillet et al.[2] focused on optimizing the parameters of the $\gamma - Re_\theta$ turbulence model. Their study involved a detailed adjustment of parameters to improve the accuracy of transition predictions in various flow conditions, underscoring the necessity for precise parameter calibration. Venkatachari et al.[30] introduced modifications to the $\gamma - Re_\theta$ turbulence model by incorporating compressibility corrections, which significantly improved prediction accuracy, particularly for transonic flows where compressibility stabilizes Tollmien-Schlichting (TS) waves. Other research involved coupling stability analysis tools with RANS solvers, as demonstrated by Venkatachari et al. [31] with

the NASA OVERFLOW CFD solver and the LASTRAC stability analysis tool. Their method proved robust in capturing various transition mechanisms across different aerodynamic configurations, though the computational cost increased due to the iterative data exchange between tools required to refine transition location predictions.

In recent years, novel data-driven approaches have emerged for enhancing transition models, with inverse modeling playing a crucial role. For example, Duraisamy et al.[9] and Duraisamy and Durbin[8] propose a new method that combines inverse modeling with machine learning to construct an intermittency transport-based model for bypass transition. Their approach utilizes adjoint-based optimization to extract intermittency data from experimental results, which are then converted into modeling knowledge through machine learning. This method shows promise in addressing inconsistencies in traditional models by optimizing data extraction and applying these insights to improve RANS transition predictions. Zafar et al. [33] introduce a recurrent neural network (RNN) model that enhances the prediction of laminar-turbulent transition in boundary layer flows. This model uses convolutional neural networks (CNNs) to predict the N factor envelope and transition locations over two-dimensional airfoils.

Previous efforts to improve RANS transition models can be grouped into two main approaches: augmenting existing models and developing new ones. Augmenting models typically involves adding or modifying terms within the existing equations, while new models are often tailored to address specific problems. Although augmenting approaches benefit from the general applicability of the original model, they often fail to fully exploit its potential due to the challenges associated with parameter calibration.

This work seeks to improve the prediction accuracy of RANS transition models by using a data-driven approach that leverages deep neural networks to fine-tune state-of-the-art transition models. By utilizing data generated from commercial CFD software, the proposed tool is trained to accurately reproduce skin friction coefficients for various two-dimensional flat plate transitional flows, using the tunable parameters of a specific RANS transition model as input features. Once trained, the model solves an inverse problem to identify the optimal set of parameters that best match the reference data. To the best of the authors' knowledge, this deep learning-based tool is the first to automate and enhance the parameter calibration of RANS transition models without altering their foundational structure or adding new terms, significantly reducing the need for manual adjustments and improving model accuracy for specific real-world applications.

2 METHODOLOGY

2.1 RANS transition model

The proposed framework is applicable to all RANS transition models and even standard RANS turbulence models. For this study, the one-equation γ model developed by Menter in 2015 [18] was chosen due to its simplicity and availability in the commercial software Star-CCM+, which was used for data generation.

2.1.1 1-Equation Gamma Transition Model

The 1-Equation γ transition model [18] was calibrated using a broad range of Falkner-Skan flows and then applied to various test cases. The goal was not to achieve perfect agreement with experimental data across all scenarios, as that would result in a highly complex set of correlations,

akin to those found in the $\gamma - Re_\theta$ model. Instead, the approach focused on carefully calibrating the model for self-similar flows (the Falkner-Skan family) and then extending this calibration with minimal added complexity to handle non-equilibrium flows, particularly those involving separation.

The transport equation for intermittency, γ, is similar to that in the $\gamma - Re_\theta$ model:

$$\frac{\partial(\rho\gamma)}{\partial t} + \frac{\partial(\rho u_j \gamma)}{\partial x_j} = \frac{\partial}{\partial x_j}\left[\left(\mu + \frac{\mu_t}{\sigma_\gamma}\right)\frac{\partial \gamma}{\partial x_j}\right] + P_\gamma - E_\gamma, \tag{1}$$

where ρ is the density, t is the time, x_j represents a coordinate, u_j is the velocity in the direction of x_j, μ is the dynamic viscosity of the fluid, μ_t is the turbulent viscosity, σ_γ is a parameter of the model, and P_γ and E_γ are the production and destruction terms, respectively. The destruction term is identical to that in the $\gamma - Re_\theta$ model:

$$E_\gamma = c_{a2}\rho W \gamma F_{\text{turb}}(c_{e2}\gamma - 1), \tag{2}$$

where c_{a2} and c_{e2} are parameters of the model, W is the modulus of the mean vorticity tensor, and F_{turb} is

$$F_{turb} = \exp\left[-(Re_T/2)^4\right], \tag{3}$$

where Re_t is the turbulent Reynolds number given by

$$Re_T = \frac{k}{\nu\omega}, \tag{4}$$

being k the turbulent intensity and nu the kinematic viscosity. The transition source term is simplified to:

$$P_\gamma = F_{\text{length}}\rho S \gamma(1-\gamma)F_{\text{onset}}, \tag{5}$$

where S is the strain rate magnitude, the transition length function, F_{length}, is no longer a correlation but a constant

$$F_{\text{length}} = 100, \tag{6}$$

and F_{onset} is a function defined next. The intermittency production term is designed to be zero in the laminar boundary layer upstream of the transition and activates once the local transition onset criteria are met.

The transition onset is controlled by the following functions:

$$F_{\text{onset}} = \max(F_{\text{onset2}} - F_{\text{onset3}}, 0), \tag{7}$$

$$F_{\text{onset2}} = \min(F_{\text{onset1}}, 2), \tag{8}$$

$$F_{\text{onset1}} = \frac{Re_v}{C_{\text{onset1}} Re_{\theta_c}}, \tag{9}$$

$$F_{\text{onset3}} = \max\left[1 - \left(\frac{Re_T}{3.5}\right)^3, 0\right], \tag{10}$$

where C_{onset1} is a parameter of the model, Re_v is the strain rate Reynolds number given by

$$Re_v = \frac{\rho d_\omega^2 S}{\mu}, \tag{11}$$

where d_ω is the wall distance, ω is the specific dissipation rate. And Re_{θ_c} is the critical momentum thickness Reynolds number, defined as a function of turbulence intensity (Tu_L) and other variables, contained inside the pressure gradient parameter λ_{θ_L}, i.e.,

$$Re_{\theta_c} = f(Tu_L, \lambda_{\theta_L}). \tag{12}$$

The main change from the $\gamma - Re_\theta$ model is that the arguments Tu_L and λ_{θ_L}, used in the correlation for Re_{θ_c}, are now approximated locally, eliminating the need for a second transport equation for Re_θ and ensuring Galilean invariance. The turbulence intensity is formulated as

$$Tu_L = \min\left(100\frac{\sqrt{2k/3}}{\omega d_w}, 100\right), \tag{13}$$

where ωd_w provides a velocity scale inside the boundary layer, replacing the free stream velocity used in the $\gamma - Re_\theta$ model,

$$U \sim S d_w \sim \omega d_w. \tag{14}$$

The pressure gradient parameter typically used in empirical correlations is defined as

$$\lambda_\theta = -\frac{\theta^2}{\mu}\frac{1}{U}\frac{\mathrm{d}P}{\mathrm{d}s} = \frac{\rho\theta^2}{\mu}\frac{\mathrm{d}U}{\mathrm{d}s}, \tag{15}$$

where $\dfrac{\mathrm{d}U}{\mathrm{d}s}$ is the acceleration/deceleration in the streamwise direction at the edge of the boundary layer. The final formula for a flat plate, considering some relations, is:

$$\lambda_{\theta_L} = -7.57 \cdot 10^{-3}\frac{\mathrm{d}V}{\mathrm{d}y}\frac{d_w^2}{\nu} + 0.0128. \tag{16}$$

For numerical robustness, λ_{θ_L} is bounded as:

$$\lambda_{\theta_L} = \min(\max(\lambda_{\theta_L}, -1.0), 1.0). \tag{17}$$

The critical momentum thickness Reynolds number, Re_{θ_c}, is computed algebraically using local variables:

$$Re_{\theta_c}(Tu_L, \lambda_{\theta_L}) = C_{TU1} + C_{TU2}\exp\left[-C_{TU3}\, Tu_L\, F_{PG}(\lambda_{\theta_L})\right], \tag{18}$$

where C_{TU1}, C_{TU2}, and C_{TU3} are parameters of the model whose effect is stated in Table 2. The function $F_{PG}(\lambda_{\theta_L})$ adjusts the sensitivity of transition onset to the stream-wise pressure gradient, calibrated using the Falkner-Skan profiles.

$$F_{PG}(\lambda_{\theta_L}) = \begin{cases} \min(1 + C_{PG1}\lambda_{\theta_L}, C_{PG1}^{lim}) & \text{if } \lambda_{\theta_L} \geq 0 \\ \min(1 + C_{PG2}\lambda_{\theta_L} + C_{PG3}\min[\lambda_{\theta_L} + 0.0681, 0], C_{PG2}^{lim}) & \text{if } \lambda_{\theta_L} < 0. \end{cases} \tag{19}$$

A limiter is applied to F_{PG} to avoid negative values:

$$F_{PG} = \max(F_{PG}, 0). \tag{20}$$

The pressure gradient correction constants are presented in Table 1.

C_{PG1}	C_{PG2}	C_{PG3}	C_{PG1}^{lim}	C_{PG2}^{lim}
14.68	-7.34	0.0	1.5	3.0

Table 1: Pressure gradient correction constants.

The coupling mechanism is similar to the $\gamma - Re_\theta$ model:

$$\frac{\partial}{\partial t}(\rho k) + \frac{\partial}{\partial x_j}(\rho u_j k) = \frac{\partial}{\partial x_j}\left[(\mu + \sigma_k \mu_t)\frac{\partial k}{\partial x_j}\right] + \widetilde{P}_k + P_k^{lim} - \widetilde{D}_k + S_k, \tag{21}$$

$$\frac{\partial}{\partial t}(\rho \omega) + \frac{\partial}{\partial x_j}(\rho u_j \omega) = \alpha \frac{P_k}{\nu_t} - D_\omega + Cd_\omega + \frac{\partial}{\partial x_j}\left((\mu + \sigma_\omega \mu_t)\frac{\partial \omega}{\partial x_j}\right), \tag{22}$$

$$\widetilde{P}_k = \gamma P_k, \tag{23}$$

$$\widetilde{D}_k = \max(\gamma, 0.1) \cdot D_k, \tag{24}$$

$$\mu_t = \rho \frac{a_1 \cdot k}{\max(a_1 \cdot \omega, F_2 \cdot S)}, \tag{25}$$

where P_k and D_k are the production and destruction terms from the turbulent kinetic energy equation in the original $k - \omega$ SST turbulence model, S_k is a source term, and Cd_ω is the cross-diffusion term. The P_k term is computed using the Kato-Launder formulation.

An additional production term, P_k^{lim}, is introduced into the k-equation to ensure proper generation of k at transition points for very low (down to zero) turbulence intensity levels. This term activates when the transition model triggers an increase in γ beyond 0.2 and deactivates in fully turbulent regions where $\mu_t > 3C_{SEP}\mu$:

$$P_k^{lim} = 5C_k \max(\gamma - 0.2, 0)(1 - \gamma) F_{on}^{lim} \max(3C_{SEP}\mu - \mu_t, 0) S\Omega, \tag{26}$$

$$F_{on}^{lim} = \min\left[\max\left(\frac{Re_v}{C_{onset1} \cdot Re_{\theta_c}^{lim}} - 1, 0), 3\right)\right], \tag{27}$$

$$Re_{\theta_c}^{lim} = 1100, \tag{28}$$

$$C_k = 1.0, \tag{29}$$

$$C_{SEP} = 1.0. \tag{30}$$

The boundary conditions for the intermittency equation are:

$$\gamma_{\text{inlet}} = 1, \tag{31}$$

$$\left.\frac{\partial \gamma}{\partial n}\right|_{\text{wall}} = 0. \tag{32}$$

Note that $\gamma_{\text{wall}} = 1/C_{e2}$, similar to the $\gamma - Re_\theta$ model.

The key parameters of the one-equation gamma model by Menter [18] and their computational effects are summarized in Table 2.

Constants	Original Value	Effect
σ_f	1.0	Increases the influence of the second derivative of the intermittency.
C_{a2}	0.06	Increases the influence of the destruction of intermittency.
C_{e2}	50.0	Increases the influence of the destruction of intermittency when the intermittency increases.
C_{TU1}	100.0	Defines the minimal value of the critical Re_{θ_c} number (for very high Tu_L levels, the exponential approaches zero).
C_{TU2}	1000.0	Defines the maximal value of the critical Re_{θ_c} number (for very low Tu_L levels, the exponential approaches one).
C_{TU3}	1.0	Controls how fast Re_{θ_c} decreases as the turbulence intensity Tu increases.
C_{onset1}	2.2	Affects the production of intermittency.
F_{length}	100	Increases proportionally the production of intermittency.

Table 2: Constants of the One-Equation Gamma Model by Menter [18] with their original values and computational effects.

2.2 Transition onset important variables

The accurate prediction of the onset of the transition in the boundary layers is critically influenced by several key variables, namely the intensity of the turbulence, the velocity of the free stream and the turbulent viscosity ratio. These variables play a pivotal role in determining the flow characteristics and the point at which the transition from laminar to turbulent flow occurs.

2.2.1 Free stream velocity

The free stream velocity, U_∞, is a crucial factor influencing the onset of the transition. Higher free stream velocities generally increase the Reynolds number, which can lead to an earlier transition due to the greater shear forces acting on the boundary layer. This relationship underscores the importance of accurately measuring and incorporating the velocity of the free stream in transition models to accurately predict the location of the onset. This variable is included in the model by means of the Reynolds number based on the characteristic length, L, i.e.,

$$Re_L = \frac{\rho U_\infty L}{\mu}. \tag{33}$$

2.2.2 Turbulence intensity

Turbulence intensity, Tu, is a measure of the fluctuations in the velocity field relative to the mean flow, i.e.,

$$Tu = \frac{u'}{U_\infty}. \tag{34}$$

It significantly impacts the onset of transition by affecting the stability of the laminar boundary layer. High turbulence intensity can induce an earlier transition by affecting disturbances

within the boundary layer, leading to an earlier breakdown to turbulence. In contrast, a lower turbulence intensity tends to delay the onset of the transition, maintaining laminar flow over a longer distance. In this work, isotropic turbulence is assumed so that the inlet turbulence kinetic energy can be obtained from the experimental inlet free stream turbulence level, and thus,

$$k = \frac{3}{2} T u^2 U_\infty^2, \tag{35}$$

where k is the turbulence kinetic energy, and U_∞ is the free stream or inlet velocity magnitude.

2.2.3 Turbulence viscosity ratio

The turbulent viscosity ratio, defined as the ratio of turbulent viscosity to molecular viscosity, i.e.,

$$TVR = \frac{\mu_t}{\mu}, \tag{36}$$

is essential in characterizing the mixing and momentum transfer within the turbulent boundary layer. A higher turbulent viscosity ratio indicates a more vigorous turbulent mixing process, which can facilitate an earlier transition by promoting instability within the laminar boundary layer. Therefore, the turbulent viscosity ratio helps to capture the complex interplay between the laminar and turbulent-flow regions.

2.3 Transition modeling problem

2.3.1 ERCOFTAC T3 flat plate

The ERCOFTAC T3 Flat Plate transitional boundary layer experiments [5] are a crucial resource for studying transitional flow phenomena. Conducted by the European Research Community on Flow, Turbulence, and Combustion (ERCOFTAC), these experiments provide a meticulously curated dataset on the behavior of boundary layers over a flat plate under various controlled conditions. The primary objective of the T3 series is to offer high-fidelity data that capture the complexities of the laminar-to-turbulent transition, a phenomenon that significantly impacts aerodynamic performance and efficiency in fluid dynamics.

In these experiments, the flat plate boundary layer is subjected to a range of free stream conditions, including variations in velocity, turbulence intensity, and pressure gradients. The dataset comprises three zero-pressure gradient (ZPG) cases (T3A, T3B, and T3A-) and five non-zero-pressure gradient (NZPG) cases (T3C1, T3C2, T3C3, T3C4, and T3C5). It includes comprehensive measurements of velocity profiles, wall shear stress, and turbulence characteristics, which are vital for understanding the mechanisms driving the transition phenomenon. This detailed data is crucial for validating and calibrating transition models within computational fluid dynamics (CFD) frameworks.

The computational domain for the T3 cases (see Figure 1) consists of a 2 meter long bottom wall and a variable height upper wall, which at the entrance has a height of 0.22 m. Following the methodology adopted Suluksna et al. [26], the computational domain extends 0.15 m upstream of the plate leading edge to eliminate interferences between the inlet and the plate. For reproducibility, the upper wall contours, h, for the NZPG cases are chosen to be the same as those provided by Suluksna et al. [26], defined as

$$h/D = \min\left[1.356x^6 - 7.591x^5 + 16.513x^4 - 17.510x^3 + 9.486x^2 - 2.657x + 0.991; 1\right] \tag{37}$$

for the T3C4 case, and

$$h/D = \min\left[1.231x^6 - 6.705x^5 + 14.061x^4 - 14.113x^3 + 7.109x^2 - 1.900x + 0.950; 1\right] \quad (38)$$

for the rest of T3C cases, where $D = 0.22$ m. These expressions reproduce the same pressure

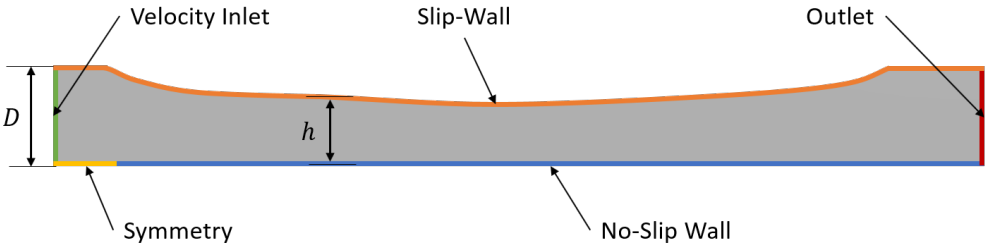

Figure 1: T3 NZPG computational domain with boundary conditions.

gradient as in the experiments by imposing the local free stream velocity according to the continuity equation. The wall contour distributions and local free stream velocity values are presented in Figure 2. For the Zero-Pressure Gradient (ZPG) cases, the domain has the same

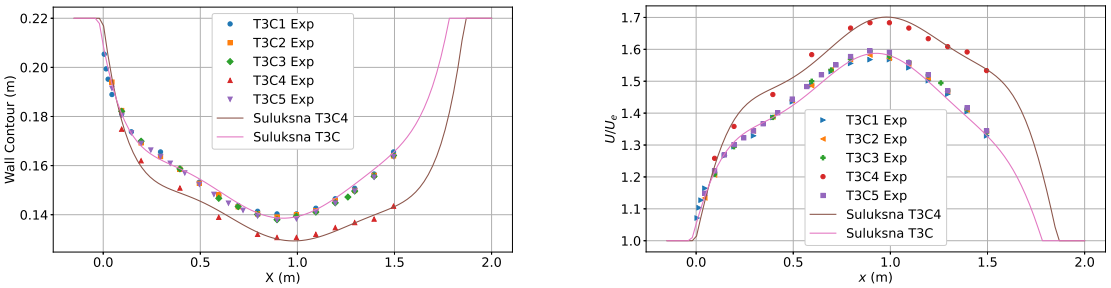

(a) Wall contours.

(b) Exterior velocity distributions.

Figure 2: Wall contours and exterior velocity distributions for the NZPG transitional flat plate cases.

dimensions and boundary conditions, but the upper wall now forms a rectangular domain with a height of $D = 0.22$ m.

The T3 series of experiments is summarized in Table 3, alongside the Schubauer-Klebanoff [25] (TSK) case, where U_∞, Tu_∞, and TVR_∞ represent the inlet, velocity, turbulence intensity, and turbulent viscosity ratio, respectively. These are the boundary conditions of the CFD simulation. The turbulence intensity at the leading edge of the plate, Tu_{LE}, is also listed. The appropriate free stream turbulence values are obtained by least-square curve fits based on the analytical decay laws derived from the $k-\omega$ SST turbulence model for the ZPG cases and numerically for the NZPG cases. As an example, Figure 3 shows the free stream turbulence decay for the T3A case.

Case	U_∞ [m/s]	Tu_∞ [%]	Tu_{LE} [%]	TVR_∞	Pressure Gradient
T3A	5.4	5.70	3.36	13.25	ZPG
T3B	9.4	8.46	6.09	100.53	ZPG
T3A-	19.8	1.12	0.94	8.0	ZPG
TSK	50.1	0.03	0.03	1.0	ZPG
T3C1	5.9	7.78	6.6	44.0	NZPG
T3C2	5.0	3.10	3.0	9.0	NZPG
T3C3	3.7	3.10	3.0	6.0	NZPG
T3C4	1.2	3.10	3.0	2.5	NZPG
T3C5	8.4	3.70	3.0	15.0	NZPG

Table 3: T3 Transitional Flat Plate Series of experiments and TSK case.

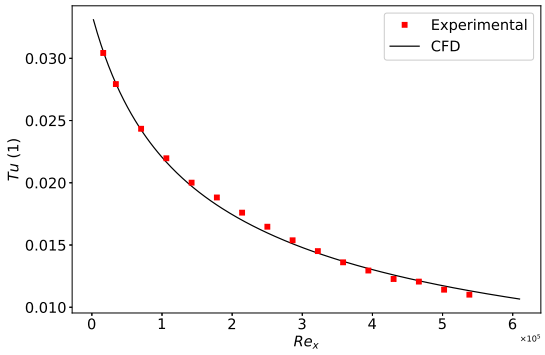

Figure 3: Free stream turbulence intensity decay from the leading edge of the plate for the T3A case.

The simulation considers incompressible flow with a density $\rho = 1.2$ kg/m^3 and dynamic viscosity $\mu = 1.8 \times 10^{-5}$ Pa s. Second-order schemes, along with a low-y^+ treatment requiring near-wall cells to be in the viscous sublayer, are employed in this work.

2.4 Machine learning

Machine learning is a powerful tool for solving optimization problems, especially because neural networks are inherently differentiable and, once trained, can substantially reduce simulation run-times. In this work, we propose utilizing a deep neural network (DNN) that leverages local variables to address the coefficient optimization problem in transition models. The framework employed in this study is depicted in Figure 4.

The input feature vector from Figure 4, denoted as $\xi = (a_i, \ldots, a_M)$, consists of the coefficients of the RANS transition model.

This vector, ξ, is fed into a deep neural network, DNN_θ, where θ represents the parameters of the network. The model is trained to predict the distribution of the skin friction coefficient along the wall. However, since the input vector lacks variables that distinguish between different flat plate cases—such as free stream velocity, free stream turbulence intensity, free stream turbulent viscosity ratio, and imposed pressure gradient—an individual model must be trained and evaluated for each flat plate case.

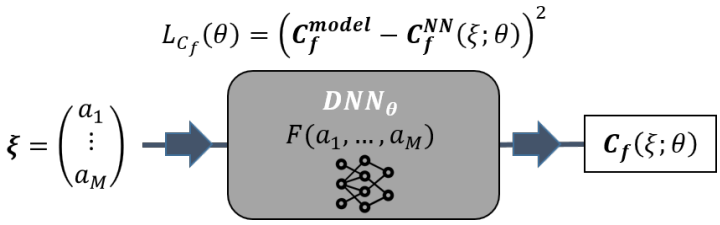

Figure 4: Direct problem framework.

As depicted in Figure 4, the neural network, which maps the transition model parameters to the skin friction coefficient, is trained using a mean squared error (MSE) function. This approach allows the network to learn from the CFD data effectively.

2.4.1 Neural network

The neural network employed in this work is a simple multilayer perceptron (MLP). Figure 5 shows schematically the structure of an MLP with the input vector ξ, two hidden layers with 4 neurons per layer, and the discretized vector $\mathbf{C_f}$ as the output.

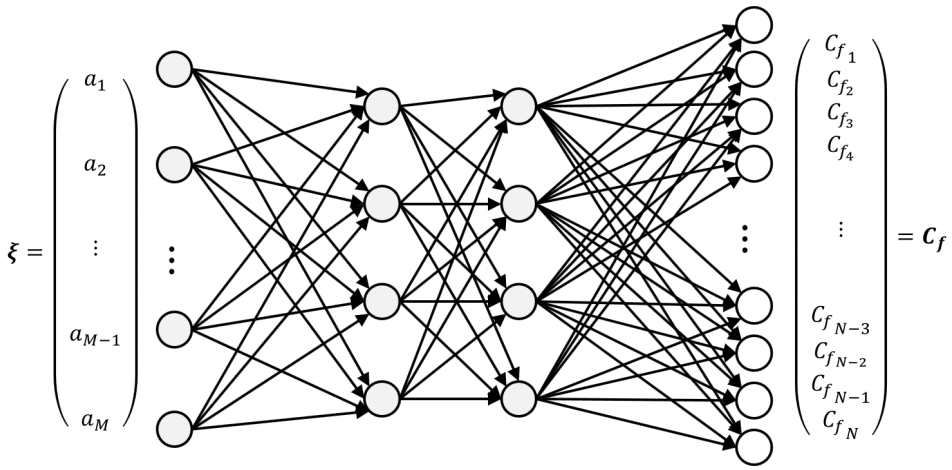

Figure 5: Multi-Layer Perceptron illustration with N input features, ξ, two hidden layers with 4 neurons per layer, and M outputs, $\tau_{\mathbf{w}}$.

After conducting hyperparameter optimization with the Ray Tune package [23] across 50 sample experiments, the optimal neural network architecture was determined to consist of 8 hidden layers, each containing 128 neurons, with an initial learning rate set to 0.0008. A scheduler was implemented to reduce the learning rate by a factor of 0.5862 every 7,900 epochs. The data was fed to the neural network in batches of 256 simulations.

All features and outputs were normalized using Z-score normalization based on the statistics of the training dataset, meaning the data was standardized by subtracting the mean and dividing by the standard deviation to achieve a normalized distribution with a mean of zero and a standard deviation of one. The training process utilized the mean squared error as the loss function and employed the ADAM optimizer [7]. The neural network used tanh activation

functions for the hidden layers. The loss function did not include any regularization terms and was initialized using the Xavier method [11].

2.5 Inverse modeling

Inverse modeling, or inverse problem-solving, is a mathematical and computational technique used to deduce the underlying parameters or causes of a system based on observed data. Unlike forward modeling, where outcomes are predicted based on a given set of parameters, inverse modeling works in reverse, aiming to identify the parameters that lead to the observed outcomes.

In this context, once the direct problem has been addressed using a deep neural network as described in Section 2.4, and the neural network is capable of mapping the input vector composed of variables influencing the transition, the inverse problem can be approached. This involves identifying the transition model parameters that cause the CFD output to align with the observed skin friction distribution.

2.5.1 Optimization procedure

Solving the inverse problem becomes an optimization task that can be addressed using the same backpropagation algorithm employed in training the neural network. The workflow is shown in Figure 6. Starting with an initial guess of the parameters, using the default set

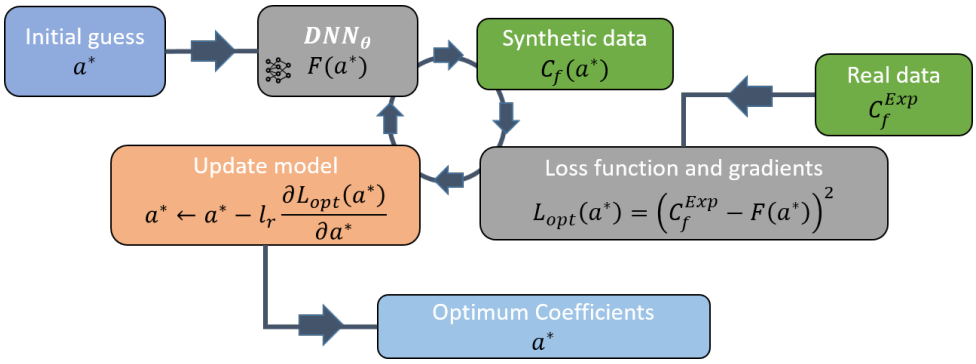

Figure 6: Inverse problem framework.

suggested by Menter [18], the deep neural network generates a prediction for the skin friction coefficient. This prediction is then evaluated using a loss function that incorporates experimental data. The gradient of the loss function with respect to the transition model coefficients is calculated, and the coefficients are iteratively updated until the optimal set is obtained.

3 RESULTS

3.1 Data generation

The dataset was generated using a Latin-Hypercube Sampling [14] (LHS) technique by specifying the number of simulations and the variation range for each RANS transition model parameter relative to their original values as defined by Menter [18]. The setups defined by the LHS were then implemented in the commercial software Star-CCM+ using Java macros, and simulations were run until asymptotic convergence of the drag coefficient was achieved. The criterion

for assessing asymptotic convergence was that the absolute difference between the maximum and minimum drag coefficient monitor values over the last 200 iterations must not exceed 10^{-6}, i.e.,

$$|\max(C_D) - \min(C_D)| < 10^{-6}, \tag{39}$$

where C_D represents the drag coefficient monitor over the last 200 iterations. Any simulation that failed to meet this criterion was excluded from the dataset. In this case, all simulations successfully achieved asymptotic convergence.

3.1.1 Mesh convergence study

The neural network requires discrete outputs, which can be reliably achieved when the simulation has reached mesh convergence. As noted by Menter et al. [17], mesh requirements depend not only on the specifics of the problem but also on the transition model used. The impact of simultaneously varying the streamwise grid resolution and the boundary layer resolution, while maintaining the same first-cell height constant for all the meshes. Furthermore, the effect of increasing the boundary layer resolution by reducing the height of the first cell is evaluated in the one-equation model γ. These effects on mesh convergence are illustrated for the T3A case in Figure 7 using the meshes detailed in Tables 4 and 5.

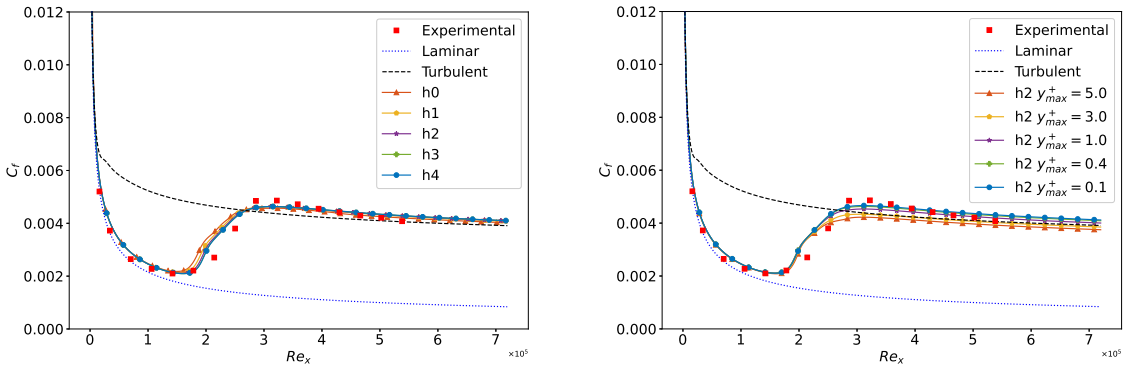

(a) T3A: Streamwise resolution effect.

(b) T3A: Wall-normal resolution effect.

Figure 7: Effect of streamwise and wall-normal resolution on transition prediction for the T3A flat plate boundary layer using the one-equation γ transition model.

To ensure consistency and accuracy across all T3 cases, the same wall resolution is maintained, allowing the neural network to eventually learn from all cases simultaneously. This approach leads to an exceptionally well-resolved boundary layer flow in all simulations, ensuring the correct application of the low-y^+ treatment and achieving convergence with sufficient numerical precision. For the subsequent results, the mesh $h2$ from Table 4 (identical to the mesh h2_3 from Table 5) demonstrates clear convergence and is therefore selected to generate the dataset.

3.1.2 Dataset description

The parameters of the transition model were varied within a range of ±50% relative to their original values listed in Table 2, resulting in a dataset comprising 2,048 simulations. Table 6

Grid	h0	h1	h2	h3	h4
Target Surface Size ($\cdot 10^3$)	$2.93L_{ref}$	$1.55L_{ref}$	$1.01L_{ref}$	$0.51L_{ref}$	$0.31L_{ref}$
Wall Surface Elements	268	534	1,068	2,134	4,268
Volume Elements	18,472	48,848	123,329	410,035	1,186,779
Prism Layers	40	70	100	175	260
Near-Wall Thickness ($\cdot 10^6$)	$5.62L_{ref}$	$5.62L_{ref}$	$5.62L_{ref}$	$5.62L_{ref}$	$5.62L_{ref}$
Prism Layer Height ($\cdot 10^3$)	$19.35L_{ref}$	$19.35L_{ref}$	$19.35L_{ref}$	$19.35L_{ref}$	$19.35L_{ref}$

Table 4: Grid convergence study for transitional flat plate case T3A, varying the streamwise mesh resolution.

Grid	h2_0	h2_1	h2_2	h2_3	h2_4
Target Surface Size ($\cdot 10^3$)	$1.01L_{ref}$	$1.01L_{ref}$	$1.01L_{ref}$	$1.01L_{ref}$	$1.01L_{ref}$
Wall Surface Elements	1,068	1,068	1,068	1,068	1,068
Volume Elements	71,338	79,320	100,490	124,981	147,258
Prism Layers	51	59	78	100	120
Near-Wall Thickness ($\cdot 10^6$)	$93.74L_{ref}$	$56.24L_{ref}$	$18.75L_{ref}$	$5.62L_{ref}$	$1.87L_{ref}$
Prism Layer Height ($\cdot 10^3$)	$19.35L_{ref}$	$19.35L_{ref}$	$19.35L_{ref}$	$19.35L_{ref}$	$19.35L_{ref}$

Table 5: Grid convergence study for transitional flat plate case T3A, varying the wall-normal resolution (meshes with different y^+_{max}).

provides various statistical measures for each parameter of the 1-Equation γ transition model within this generated dataset.

	σ_f	$Ca2$	$Ce2$	$CTU1$	$CTU2$	$CTU3$	$Conset1$
Default Value	1	0.06	50	100	1000	1	2.2
Mean	1.00	0.06	49.65	100.62	1002.26	1.00	2.19
Standard Deviation	0.29	0.017	14.40	28.63	289.88	0.29	0.64
Skewness	-1.33e-04	1.25e-05	6.50e-05	1.61e-04	-1.34e-04	-1.35e-04	-1.36e-05
Kurtosis	-1.20	-1.20	-1.20	-1.20	-1.20	-1.20	-1.20

Table 6: Dataset Generation statistics for each of the parameters of the 1-Equation Gamma transition model.

3.1.3 Dataset split

The dataset was randomly split into training (80%), validation (10%), and test (10%) subsets. The training dataset is used to determine the network's parameters, specifically the weights and biases. The validation dataset helps prevent overfitting and assists in tuning the network's hyperparameters. Finally, the test dataset evaluates the model's accuracy on unseen data. It is crucial that the distributions of these three subsets are statistically similar and have comparable point concentrations. Figure 8 compares the violin plots for each input feature of the neural network, confirming that the datasets are sufficiently similar in their distributions.

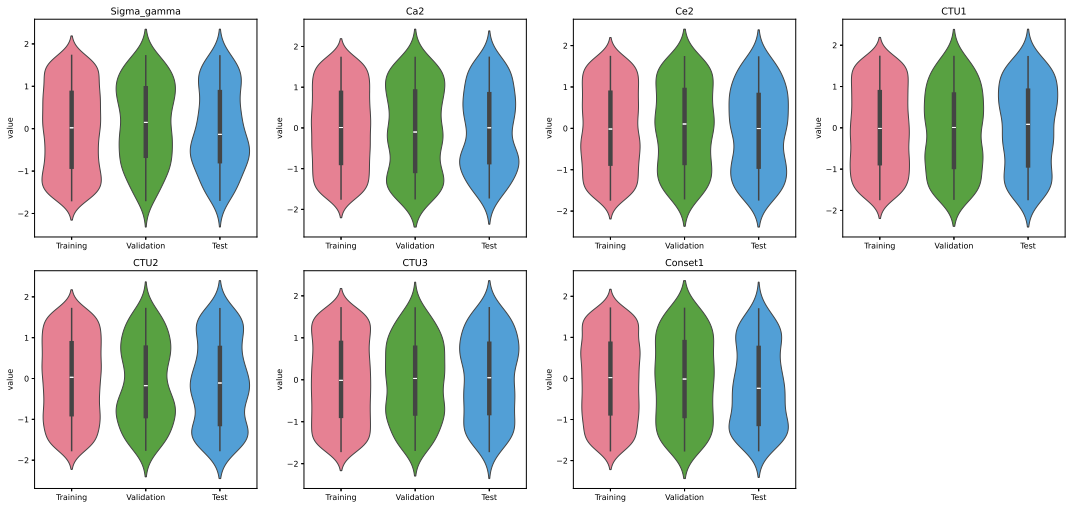

Figure 8: Violin plots comparing the distribution of input features for the selected random split.

3.2 Training and validation

To enhance the efficiency of both training and subsequent optimization, discretized skin friction coefficient points with a standard deviation across the training dataset lower than a threshold of 0.0001 were removed from the data. This step ensures that the model focuses on learning data that is meaningfully correlated with the input features. When the variation in the outputs is minimal, it indicates that these outputs are not strongly dependent on the inputs and thus provide little value for the network.

The training and validation phases used 1,536 and 256 simulations of the T3A case, respectively. The entire process took approximately 30 minutes on a machine with 4 CPUs and no GPUs. Training and validation losses are depicted in Figure 9. The spikes in the loss curves are

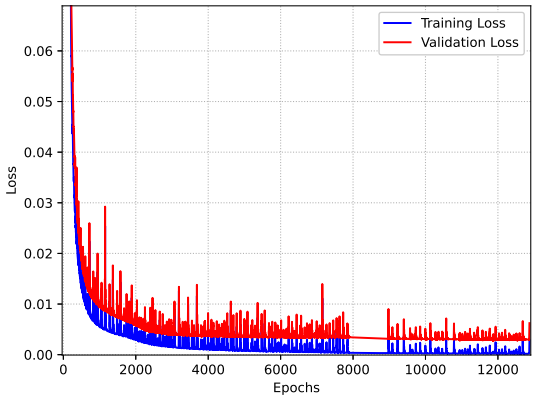

Figure 9: Training and validation loss curves behavior for T3A case.

intrinsic to the ADAM optimizer [34], and the training is "early stopped" when the validation

loss starts to increase.

3.3 Test

Once the model is trained, its accuracy can be evaluated using a test dataset consisting of 256 simulations. Figure 10 illustrates a comparison between randomly selected setups from the test dataset and the corresponding model predictions. It is important to note the point at which the model begins to accurately predict the skin friction coefficient; earlier points were excluded from consideration due to their very low standard deviation across the simulations (see Section 3.2).

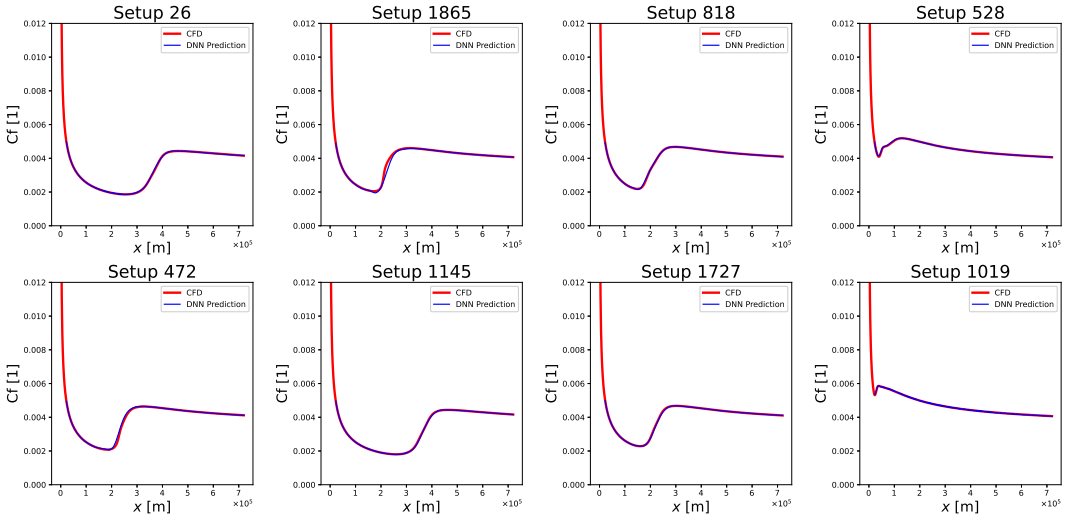

Figure 10: Comparison of skin friction distributions for randomly sampled setups within the test dataset.

Figure 11 presents a scatter plot of the true values versus the predicted values, with a color legend representing the relative error. The model's coefficient of determination (R^2), which quantifies the proportion of variability in the dependent variable, C_f, explained by the independent variables (the transition model parameters), is 0.997. This high R^2 value indicates an excellent fit of the model to the data.

3.4 Optimization

The optimization process converges quickly, taking about 5,000 iterations and only 5 minutes to complete, using the same machine as was used for training.

Figure 12 shows the skin friction coefficient distribution obtained with the default and optimized set of parameters found by the model. The DNN result captures a more accurate transition onset compared to the original set of parameters of the transition model. However, the initial and final tails of the skin friction distribution are not matched because they are not a function of the transition model parameters, but of other variables such as the parameters of the underlying $k-\omega$ SST turbulence model. The optimized set of parameters for the 1-Equation γ transition model is compared to the default set in Table 7. As anticipated for the T3A case, the parameter C_{onset1} proves to be the most influential. A slight reduction of 1.81% from its

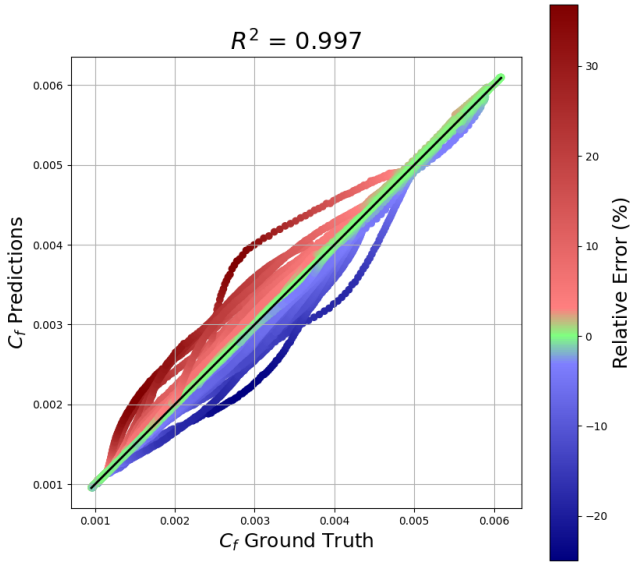

Figure 11: Scatter plot of ground truth (test) skin friction coefficients versus the predicted skin friction coefficients. The legend indicates the relative error in percentage. $R^2 = 0.997$.

	σ_f	$Ca2$	$Ce2$	$\gamma_{\min}$	$CTU1$	$CTU2$	$CTU3$	$Conset1$
Default Set	1	0.06	50	1e-10	100	1000	1	2.2
Optimized Set	0.9952	0.0596	49.7518	1e-10	101.0107	1007.6765	0.9758	2.2398
Difference	0.48 %	0.65 %	0.50 %	0 %	-1.01 %	-0.77 %	2.42 %	-1.81 %

Table 7: Optimized set of parameters for the T3A case and the 1-Equation Gamma transition model.

original value results in the onset of the transition moving downstream. In particular, the model also identified the significance of the parameter C_{TU3}, which underscores the importance of the algorithm presented in this study. This algorithm shows its practicality, as manually determining the optimal tuning configurations for each specific experiment would be an impractical and labor-intensive task.

4 CONCLUSION

In this study a deep neural network framework was developed to optimize the parameters of RANS transition models, achieving an R^2 of 0.997 in predicting skin friction coefficients for the T3A case. The optimized parameters improved model accuracy by shifting the onset of transition downstream without altering the model's foundational structure, demonstrating a novel approach to automated calibration. The model's ability to closely match experimental data highlights its potential to enhance the predictive accuracy of RANS transition models and

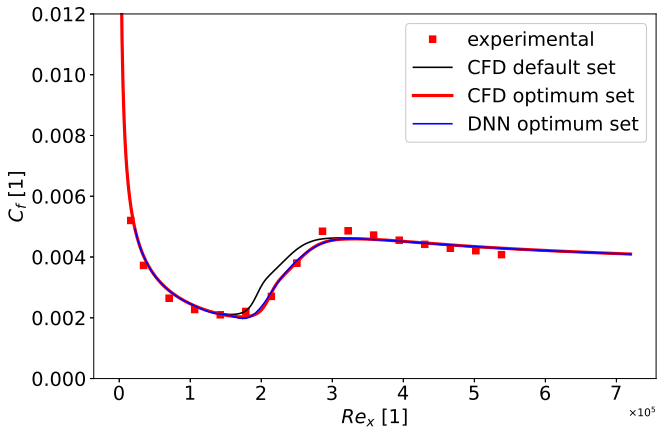

Figure 12: Comparison of skin friction distribution for the T3A case with the default and optimized set of parameters of the 1-Equation γ model.

suggests that similar deep learning-based methods could be applied to more complex geometries and flow conditions.

However, achieving a perfect match for the entire skin friction distribution was not possible, as the optimization considered only the transition model parameters. This limitation is partly due to factors such as the parameters of the underlying turbulence model, specifically the $k-\omega$ SST model.

The proposed framework is versatile and can be adapted to various models. Future work will focus on fine-tuning parameters for each flat plate experiment and extending the framework to other geometries, such as airfoils. Additionally, the inclusion of imposed pressure gradients and non-flat geometries as neural network inputs is planned, with the goal of training a model capable of predicting a global optimum across all available transitional boundary layer experiments.

This approach offers significant potential for enhancing both transition and standard turbulence models. For instance, it could enable the introduction of new terms proportional to specific parameters, which, once trained, can be fine-tuned by the neural network to enhance model capabilities.

Overall, our results demonstrate the potential of this framework to serve as a powerful tool for researchers and industry professionals, streamlining the use of RANS transition models across various applications——from aircraft design to environmental flow studies——while improving both efficiency and accuracy.

5 ACKNOWLEDGEMENTS

This project has received funding from the Spanish Ministry of Defense under grant agreement "Potenciación de Capacidades de Producción de Aeronaves: Servicios de Análisis Aerodinámico para la Ingeniería de Integración de Cargas en Aeronaves del Ejército del Aire".

The authors gratefully acknowledge the "Centro de Supercomputación y Visualización de Madrid" (CESVIMA) and Universidad Politécnica de Madrid for providing computing resources on Magerit Supercomputer.

REFERENCES

[1] Argus, F. J., G. A. Ament, and W. J. F. Koning, eds. 2020. "The Influence of Laminar-Turbulent Transition on Rotor Performance at Low Reynolds Numbers." In VFS Aeromechanics for Advanced Vertical Flight Technical Meeting.

[2] Barrouillet, B., and E. Laurendeau. 2021. "On the Calibration of the Transitional $k-\omega-\gamma-Re_{\theta_t}$ Turbulence Model." http://doi.org/10.2514/6.2021-0629

[3] Brandis, Aaron M., Christopher O. Johnston, and Brett A. Cruden. 2016. "Nonequilibrium Radiation for Earth Entry." AIAA Paper 2016-3690. http://doi.org/10.2514/6.2016-3690

[4] Chi, Y., ed. 1993. "Fluid Mechanics Proceedings." NASA SP-255.

[5] Coupland, J., ed. 1990. "ERCOFTAC Special Interest Group on Laminar to Turbulent Transition and Retransition: T3A and T3B Test Cases." A309514.

[6] Crouch, J. D. 2015. "Boundary-Layer Transition Prediction for Laminar Flow Control." In 45th AIAA Fluid Dynamics Conference, 2015-2472. Dallas, TX: AIAA. http://doi.org/10.2514/6.2015-2472

[7] Driederik, K. P. and Ba, J. 2017. "Adam: A Method for Stochastic Optimization." arXiv preprint arXiv:1412.6980. https://arxiv.org/abs/1412.6980.

[8] Duraisamy, K., and P. A. Durbin, eds. 2014. "Transition Modeling using Data Driven Approaches." https://api.semanticscholar.org/CorpusID:8626637

[9] Duraisamy, K., Z. J. Zhang, and A. P. Singh, eds. 2015. "New Approaches in Turbulence and Transition Modeling Using Data-Driven Techniques." https://api.semanticscholar.org/CorpusID:62007605

[10] Dornheim, Michael A. 1996. "Planetary Flight Surge Faces Budget Realities." Aviation Week & Space Technology 145, no. 24: 44–46.

[11] Glorot, Xavier, and Yoshua Bengio. 2010. "Understanding the Difficulty of Training Deep Feedforward Neural Networks." In *Proceedings of the Thirteenth International Conference on Artificial Intelligence and Statistics*, edited by Yee Whye Teh and Mike Titterington, 249–256. Chia Laguna Resort, Sardinia, Italy: PMLR, May 13–15. http://proceedings.mlr.press/v9/glorot10a/glorot10a.pdf.

[12] Richez, F., A. Nazarians, and C. Lienard, eds. 2017. "Assessment of Laminar-Turbulent Transition Modeling Methods for the Prediction of Helicopter Rotor Performance." In 43rd European Rotorcraft Forum, Milan, Italy.

[13] Joslin, R. D. 1998. "Overview of Laminar Flow Control." NASA TP-1998-208705. Washington, DC: NASA.

[14] McKay, M. D. 1992. "Latin Hypercube Sampling as a Tool in Uncertainty Analysis of Computer Models." In *Proceedings of the 24th Conference on Winter Simulation (WSC '92)*, 557–564. December 1. https://doi.org/10.1145/167293.167637.

[15] Menter, F. R. 1994. "Two-Equation Eddy-Viscosity Turbulence Models for Engineering Applications." AIAA Journal 32, no. 8: 1598–1605. http://doi.org/10.2514/3.12149

[16] Langtry, R. B. 2006. "A Correlation-Based Transition Model using Local Variables for Unstructured Parallelized CFD Codes." PhD diss., Institut für Thermische Strömungsmaschinen und Maschinenlaboratorium Universität Stuttgart.

[17] Menter, F. R., R. Sechner, and A. Matyushenko. 2024. "Best Practice: RANS Turbulence Modeling in Ansys CFD." RANS Turbulence Modeling in Ansys CFD 95: 62–63.

[18] Menter, F. R., P. E. Smirnov, T. Liu, and R. Avancha. 2015. "A One-Equation Local Correlation-Based Transition Model." Flow Turbulence Combust 95: 583–619. http://doi.org/10.1007/s10494-015-9622-4

[19] Menter, F. R., A. Matyushenko, R. Lechner, A. Stabnikov, and A. Garbaruk. 2022. "An Algebraic LCTM Model for Laminar–Turbulent Transition Prediction." Flow, Turbulence and Combustion 109: 841–869. http://doi.org/10.1007/s10494-022-00336-8

[20] Oates, Gordon C., ed. 1984. "Aerothermodynamics of Gas Turbine and Rocket Propulsion." AIAA Education Series. New York: AIAA.

[21] Peyret, Roger, and Thomas D. Taylor. 1983. "Computational Methods for Fluid Flow." 2nd ed. New York: Springer-Verlag.

[22] Piotrowski, M. G. H., and D. W. Zingg. 2020. "Smooth Local Correlation-Based Transition Model for the Spalart–Allmaras Turbulence Model." AIAA Journal 59. http://doi.org/10.2514/1.J059784

[23] Liaw, R., E. Liang, R. Nishihara, P. Moritz, J. E. Gonzalez, and I. Stoica. 2018. "Tune: A Research Platform for Distributed Model Selection and Training." CoRR, abs/1807.05118. http://arxiv.org/abs/1807.05118.

[24] Schneider, Steven P. 2004. "Hypersonic Laminar–Turbulent Transition on Circular Cones and Scramjet Forebodies." Progress in Aerospace Sciences 40, no. 1: 1–50. http://doi.org/10.1016/j.paerosci.2003.11.001

[25] Schubauer, G. B. and Klebanoff, P. S. "Contribution on the Mechanics of Boundary Layer Transition". NACA TN 3489 (1955).

[26] Suluksna, K., P. Dechaumphai, and E. Juntasaro. 2008. "Correlations for Modeling Transitional Boundary Layers under Influences of Freestream Turbulence and Pressure Gradient." International Journal of Heat and Fluid Flow 30: 66–75. http://doi.org/10.1016/j.ijheatfluidflow.2008.09.004

[27] Terster, W. 1997. "NASA Considers Switch to Delta 2." Space News 8, no. 2: 13–19.

[28] Thompson, C. M. 1989. "Spacecraft Thermal Control, Design, and Operation." In AIAA Guidance, Navigation, and Control Conference, CP849, 1: 103–115. Washington, DC: AIAA.

[29] Vatistas, G. H., Lin, S., and Kwok, C. K. 1986. "Reverse Flow Radius in Vortex Chambers." AIAA Journal 24, no. 11: 1872–1873. http://doi.org/10.2514/3.13046

[30] Venkatachari, B. S., P. Paredes, M. M. Choudhari, F. Li, and C. Chang, eds. 2022. "Transition Analysis for the CRM-NLF Wind Tunnel Configuration using Transport Equation Models and Linear Stability Correlations." http://doi.org/10.2514/6.2022-1542

[31] Venkatachari, B. S., J. A. Carnes, C. Chang, and M. Choudhari. 2022. "Boundary-Layer Transition Prediction Through Loose Coupling of OVERFLOW and LASTRAC." http://doi.org/10.2514/6.2022-3682

[32] Volpe, Richard. 1994. "Techniques for Collision Prevention, Impact Stability, and Force Control by Space Manipulators." In Teleoperation and Robotics in Space, edited by S. B. Skaar and C. F. Ruoff, 175–212. Washington, DC: AIAA.

[33] Zafar, M. I., M. M. Choudhari, P. Paredes, and H. Xiao. 2021. "Recurrent Neural Network for End-to-End Modeling of Laminar-Turbulent Transition." Data-Centric Engineering 2: e17. http://doi.org/10.1017/dce.2021.11

[34] Molybog, I. et al. 2023 "A theory on Adam Instability in Large-Scale Machine Learning". arXiv, cs.LG, 2304.09871. https://arxiv.org/abs/2304.09871.